

Improvements in plate anchor capacity due to cyclic and maintained loads combined with consolidation

ZEFENG ZHOU*, CONLETH D. O'LOUGHLIN†, DAVID J. WHITE‡ and SAM A. STANIER§

Plate anchor technology is an efficient solution for mooring offshore floating facilities for oil and gas or renewable energy projects. When used with a taut mooring, the anchor is typically subjected to a maintained load component and intermittent episodes of cyclic loading throughout the design life. These loads, and the associated shearing, remoulding and consolidation processes, cause changes in the anchor capacity, particularly in soft, fine-grained soils. The changing anchor capacity affects the mooring performance by changing the safety margin and also the overall system reliability. In this paper the changing anchor capacity in reconstituted, normally consolidated natural carbonate silt was assessed through a series of beam centrifuge tests on horizontally loaded circular plate anchors. The results demonstrate that full consolidation under a typical maintained load leads to a 50% gain in the anchor capacity, and subsequent cyclic loading and reconsolidation can triple this increase. An effective stress framework based on critical state concepts is employed to explain and support the experimental observations. This study shows that, when viewed from a whole-life reliability perspective, maintained and cyclic loading provide a long-term enhancement of anchor capacity in soft, fine-grained soils. This beneficial effect is currently overlooked in design practice, but can be predicted using the framework shown here, which can form the basis for a digital twin that monitors the through-life integrity of a plate anchor.

KEYWORDS: anchors & anchorages; bearing capacity; centrifuge modelling; consolidation; numerical modelling; offshore engineering; soil/structure interaction

INTRODUCTION

The offshore energy industry is increasingly reliant on floating facilities to exploit oil, gas, wind, tidal and wave energy resources. Floating facilities are kept on station using mooring lines that terminate at anchors in the seabed. When the moorings are taut, the mooring line load includes maintained and cyclic components that are resisted by a combination of the submerged weight of the mooring in the water column, the seabed friction that develops between the mooring line and the seabed and by mobilisation of soil strength around the anchor.

The loading transferred to the anchor changes the strength of the seabed around the anchor over its design life. The weakening effect of cyclic loading on soil strength is well recognised in current design practice, and methodologies for quantifying the cyclic 'fatigue' of soil are well developed (e.g. Andersen *et al.*, 1988; Andersen, 2015). However, over the operating period of the facility, dissipation of excess pore pressure will occur, which can result in a regain in soil

strength. This consolidation effect on soil strength and anchor capacity is commonly overlooked, but can be important and beneficial for design practice.

This paper considers these effects through a series of centrifuge tests and retrospective numerical simulations of an embedded plate anchor subjected to differing combinations of consolidation and cyclic load. The focus is on plate anchors, rather than pile anchors (driven, suction or gravity installed), which is motivated by their low cost and high performance (Aubeny, 2018; O'Loughlin *et al.*, 2018). For example, the follower used to install the plate anchor (e.g. a suction pile (Wilde *et al.*, 2001)), can be reused and the holding capacity of a plate is high relative to the weight of the anchor (O'Loughlin *et al.*, 2015, 2017).

Plate anchor capacity under undrained, unconsolidated seabed conditions has been well established through model testing (e.g. Gaudin *et al.*, 2006; Blake *et al.*, 2010; O'Loughlin *et al.*, 2014), medium- to large-scale field testing (e.g. Dahlberg & Strøm, 1999; Heyerdahl & Eklund, 2001; Wilde *et al.*, 2001; Blake and O'Loughlin, 2015; O'Loughlin *et al.*, 2016) and analytical and numerical modelling (e.g. Martin & Randolph, 2001; Wang *et al.*, 2010, 2013; Yu *et al.*, 2011; Wang & O'Loughlin, 2014; Liu *et al.*, 2018). This work has validated the rigorous plasticity solutions and other numerical results that can be used to link the in situ soil undrained strength to the initial monotonic bearing capacity of an embedded plate. Quantifying changes in plate anchor capacity due to the evolution of soil strength under more realistic long-term loading has received much less attention, with the exception of Wong *et al.* (2012) and Han (2016), who present experimental data of gains in capacity resulting from monotonic loading.

However, over the life of a typical floating facility, moorings experience many episodes of cyclic loading associated with changing wave or wind conditions. The background maintained load may also slowly vary,

Manuscript received 2 March 2019; revised manuscript accepted 15 November 2019. Published online ahead of print 2 January 2020. Discussion on this paper closes on 1 December 2020, for further details see p. ii.

* Centre for Offshore Foundation Systems and ARC Research Hub for Offshore Floating Facilities, University of Western Australia, Perth, WA, Australia (Orcid:0000-0002-3575-8810).

† Centre for Offshore Foundation Systems and ARC Research Hub for Offshore Floating Facilities, University of Western Australia, Perth, WA, Australia.

‡ University of Southampton, Southampton, UK and ARC Research Hub for Offshore Floating Facilities, University of Western Australia, Perth, WA, Australia.

§ University of Cambridge, Cambridge, UK and ARC Research Hub for Offshore Floating Facilities, University of Western Australia, Perth, WA, Australia.

for example with the loading or ballast condition of the floating system. As a result of this complex time-varying load, changes in anchor capacity are expected to be more significant than observed in previous experiments.

There is significant value in quantifying these changes in capacity both as part of the design process, and for asset management during operation of a moored facility. For design, the reliability of the system is affected by both improvements in performance (such as these gains in anchor capacity) as well as degradation (such as from corrosion of the mooring line). Both positive and negative effects should be considered to reach an accurate assessment of the system reliability and the true probability of failure. Meanwhile, during operation, a model that tracks the changing capacity of the anchor as a result of the environmental conditions experienced provides a basis for reassessing the mooring capacity if design inputs are altered (e.g. the maximum expected storm load is updated) or if a life extension is required. Such a model can form a 'digital twin' (Grieves & Vickers, 2017; Sharma *et al.*, 2017) of the anchor, to extend current usage of digital twinning (i.e. establishing virtual models of a physical asset) for asset management of floating systems (e.g. Renzi *et al.*, 2017).

This paper provides experimental data on the changing capacity of an embedded plate anchor in normally consolidated calcareous silt due to episodes of maintained and cyclic load. These data are simulated by way of a digital twin of the centrifuge test that uses the effective stress framework set out by Zhou *et al.* (2019a) to calculate the changing soil strength due to undrained shearing and consolidation.

EXPERIMENTAL PROGRAMME

Geotechnical centrifuge facility

The experiments were performed in the 3.6 m dia. beam centrifuge at the University of Western Australia (UWA) (Randolph *et al.*, 1991) at an acceleration level of 150g. The test programme involved four anchor tests with differing loading sequences and a suite of in-flight characterisation tests to provide geotechnical properties to assist interpretation of the anchor tests, including selection of model parameters for the analytical framework used for back-analysis. The anchor tests involved horizontal loading of a vertically oriented plate anchor (i.e. with no prescribed changes in embedment depth) with a mixture of consolidation and one-way cyclic loading phases. T-bar penetrometer tests were performed with equivalent cyclic loading phases, to explore the comparative changes in soil strength in similar penetrometer and anchor tests.

Soil sample

The soil sample was prepared from bulk samples of a natural carbonate silt retrieved from offshore Australia with geotechnical properties as summarised in Table 1. The silt was reconstituted as a slurry with a water content of 145% and poured into a sample container measuring 650 by 390 mm in plan and 325 mm deep. The sample was consolidated under self-weight in the centrifuge at an acceleration of 150g for 5 days, during which time additional slurry was added to achieve a final sample height of approximately 210 mm. A 35 mm layer of free water was maintained at the sample surface to ensure saturation. The average effective unit weight of the sample was established from moisture content determinations made on cores taken from other centrifuge samples of the same soil subjected to the same sample preparation procedures (Chang *et al.*, 2019; Chow *et al.*, 2019; Zhou *et al.*, 2019b). This was necessary as no undisturbed locations remained after the testing described

Table 1. Properties of the calcareous silt (from Chow *et al.*, 2019)

Property	Value
Liquid limit, LL: %	67
Plastic limit, PL: %	39
Specific gravity, G_s	2.71
Slope of normal consolidation line, λ	0.287
Slope of swelling line, κ	0.036
Specific volume, v , at $\sigma'_v = 1$ kPa on NCL, Γ_{NCL}	4
Carbonate content, calcium carbonate (CaCO_3): %	73.29

in this paper. Over the range of vertical effective stress levels relevant to the anchor tests, the initial moisture contents were in the range 65–88%, with an average effective unit, $\gamma' = 5.2$ kN/m³.

Model anchor and test set-up

Model anchor and load cell. The circular anchor plate was stainless steel with diameter, $D_a = 35$ mm and thickness, $t_a = 3$ mm. The projected area of the plate anchor is ~ 22 m² in equivalent prototype scale, which is within the range used in practice – for example, 16–44 m² for SEPLAs (Brown *et al.*, 2010; Cassidy *et al.*, 2012) and 7–30 m² for drag-embedded vertically loaded plate anchors (Vryhof, 2006). The anchor was loaded using a 1.2 mm dia. stainless steel wire. The applied load was measured at the anchor using a miniature load cell (6 mm dia. and 12 mm long) with a measurement range of 1.5 kN (Fig. 1). The anchor displacement was measured using the encoder located on the vertical axis of the actuator used to pull on the loading wire, with small corrections applied to account for system compliance.

Experimental arrangement and procedures. Figure 2 shows the experimental arrangement during the installation and preparation stages of the tests, which involved the following steps that were undertaken with the centrifuge stopped.

- Before installing the anchor a vertical slot was cut in the consolidated sample (using a 3 mm thick steel plate) for the anchor loading line to pass through (Fig. 2(a)). Verticality and positioning of this slot was ensured by two steel guides that were mounted on the sample container.
- A pulley arrangement was installed at one end of the sample container, with the anchor loading line and load cell cable threaded through (Fig. 2(b)).

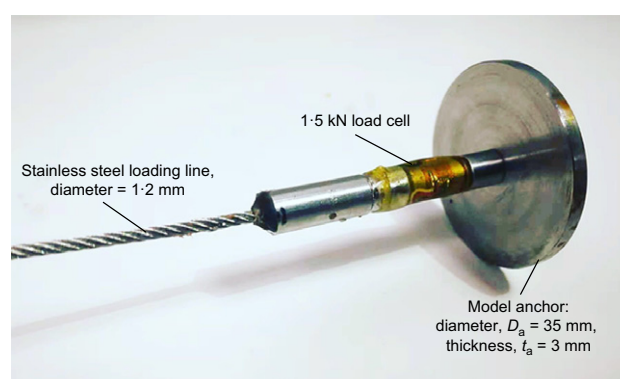


Fig. 1. Model anchor

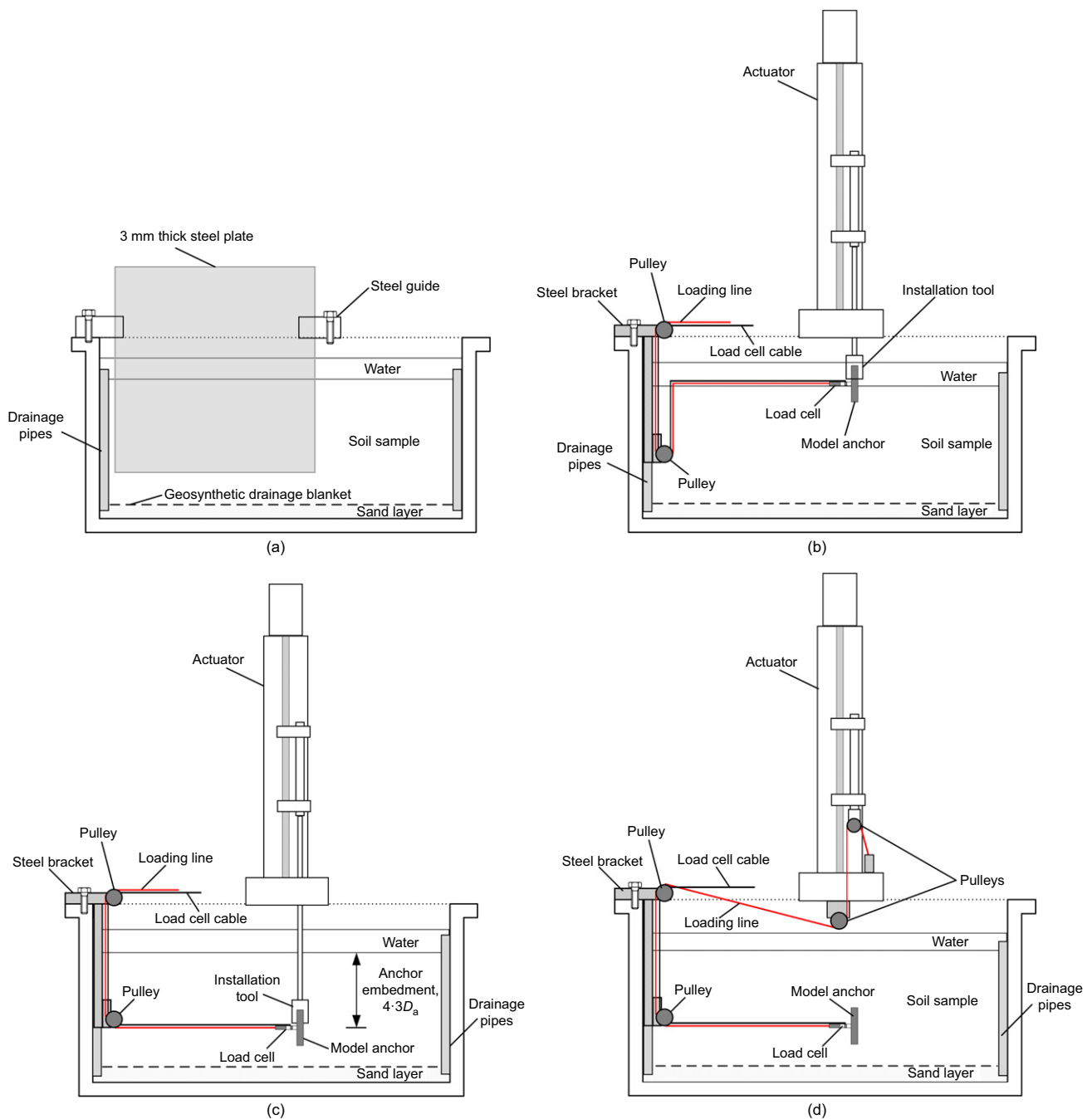


Fig. 2. Experimental arrangement at different stages: (a) cutting a slot for the anchor loading line; (b) before anchor installation; (c) after anchor installation; (d) in preparation for loading

- (c) The anchor was installed using a mandrel mounted on the vertical axis of the actuator at a penetration velocity of 0.1 mm/s (Fig. 2(c)). A slight tension was maintained on the loading line and load cell cable to ensure that they followed the anchor into the slot created in step (a).
- (d) The electrical actuator was then positioned on cross-beams spanning the width of the sample container, and the anchor loading line connected to the actuator's vertical axis, in order to apply horizontal loading to the anchor (Fig. 2(d)).

The initial anchor embedment (measured to the centre of the circular plate, see Fig. 2(d)) was $z = 150 \text{ mm}$ for all anchor tests, equivalent to $z/D_a = 4.3$. This embedment depth was selected to target a 'deep' flow-round response so that the soil deformation remained local to the anchor, rather than

reaching either the soil surface or the bottom (sand) boundary ($1.7D_a$ from the centre of the plate). Numerical simulations reported by Yu *et al.* (2015) confirm these dimensions are appropriate, aided by the strength gradient in the sample, which causes the failure mechanism to become one-sided, skewing towards the weaker soil (i.e. towards shallower depths).

By installing the anchor at $1g$ such that it would translate without rotation when loaded, it was possible to quantify the effects of cyclic loading and consolidation without the complicating effects of installation and subsequent rotation (keying) of the anchor. However, we began each test with a monotonic pull to failure, to represent in a repeatable way some level of installation-induced disturbance.

After installation of the anchor and loading system, the centrifuge was spun to $150g$ and a period of 3 h allowed

before starting the anchor test. Each anchor test involved combinations of monotonic, maintained and/or cyclic loading. Details relevant to each of these loading stages are provided below.

- Monotonic loading.** Each anchor test involved an initial monotonic stage where the anchor was loaded in displacement control at a velocity, $v_a = 1$ mm/s, such that the dimensionless group, $v_a D_a / c_{op} = 92$ (using an 'operative' coefficient of consolidation, $c_{op} = 4$ m²/year from piezo-foundation dissipation data presented later) so the response is undrained (House *et al.*, 2001; Randolph & Hope, 2004; Colreavy *et al.*, 2016). This monotonic stage was maintained until the anchor capacity became steady (which occurred within $< 2.5 D_a$ of movement). This steady anchor capacity was used as the reference undrained unconsolidated anchor capacity, $q_{a,uu}$, for defining the subsequent maintained and cyclic loading phases. A final monotonic stage was also conducted after the maintained and/or cyclic loading phase of the test, using the same velocity, $v_a = 1$ mm/s, for an anchor displacement that was sufficient to observe the peak anchor capacity.
- Maintained loading.** This stage of the anchor tests involved operating the actuator in load control to maintain an anchor resistance equal to half of that measured in the initial monotonic stage (i.e. $q_a = 0.5 q_{a,uu}$) for a period of 3 h. This consolidation period was sufficient for about 95% dissipation of excess pore pressure, as estimated using consolidation data described later.
- Cyclic loading.** The cyclic loading stage of the anchor tests involved 1080 cycles (to reflect a typical number of cycles for a 3 h design storm) of loading from $0.25 q_{a,uu}$ to $0.75 q_{a,uu}$. The frequency of the cycles was 0.4 Hz, and was selected as a balance between being able to achieve high-quality load control and ensuring undrained conditions. In a single load cycle the dimensionless time, $T = c_{op} t / D_a^2 = 0.0003$ (using $c_{op} = 4$ m²/year) and so the drainage within a single cycle was negligible.

Soil characterisation

Undrained shear strength. A model scale T-bar penetrometer (Stewart & Randolph, 1991) with a diameter, $d = 5$ mm and a length of 20 mm was used to determine profiles of intact and remoulded shear strength. Two 'standard' T-bar tests (TB_01 and TB_02) involving undrained penetration (at $v_p = 3$ mm/s such that $v_p d / c_h = 40$, where $c_h = 12$ m²/year; see Fig. 7 later in the paper) and cyclic phases gave the profiles of undrained shear strength, s_u , shown in Fig. 3(a), where s_u was interpreted using a constant T-bar capacity factor of 10.5 (Martin & Randolph, 2006). The profiles are fitted by

$$s_{u,i} = kz \quad (1)$$

where $s_{u,i}$ is the initial undrained shear strength and k is the strength gradient with (prototype) depth, z . As shown in Fig. 3(a), $k = 2$ kPa/m, which gives a normally consolidated shear strength ratio, $(s_u / \sigma'_{v0})_{NC} = 0.38$, which is slightly higher than $(s_u / \sigma'_{v0})_{NC} = 0.32$ determined from simple shear tests (Chow *et al.*, 2019). The cyclic episode of the T-bar test progressively remoulds the soil, degrading the undrained shear strength towards the fully remoulded strength, with the limiting value of $s_{u,cyc} / s_{u,i}$ indicating a soil sensitivity, $S_t \sim 5$, where S_t is the ratio between the in situ and fully remoulded undrained shear strengths (Fig. 3(b)).

The second group of T-bar tests included a cyclic episode with 1080 load-controlled cycles (i.e. equal to the cycles imposed in the anchor tests), between either $0.25 s_{u,i}$ and $0.75 s_{u,i}$ (test TB_03) or 0 and $0.75 s_{u,i}$ (test TB_04) at an initial depth, $z = 52$ mm. The cyclic load amplitude in TB_03 is consistent with the anchor tests, and TB_04 explores a higher amplitude. A loading frequency of 1 Hz ensured an undrained response within each cycle, while ensuring accurate load control. In both tests there is a local increase in soil strength after cyclic loading, with peak values of $s_u = 44.5$ kPa in TB_03 (Fig. 4(a)) and $s_u = 55$ kPa in TB_04 (Fig. 4(b)), which are about 2.5 and 2.75 times higher than the initial soil strength at the same depth.

The two groups of T-bar tests demonstrate that, although cyclic remoulding leads to a significant reduction in soil strength (TB_01 and TB_02), one-way cyclic loading to much lower shear strains but over a longer time period causes a significant gain in soil strength. This is due to dissipation of

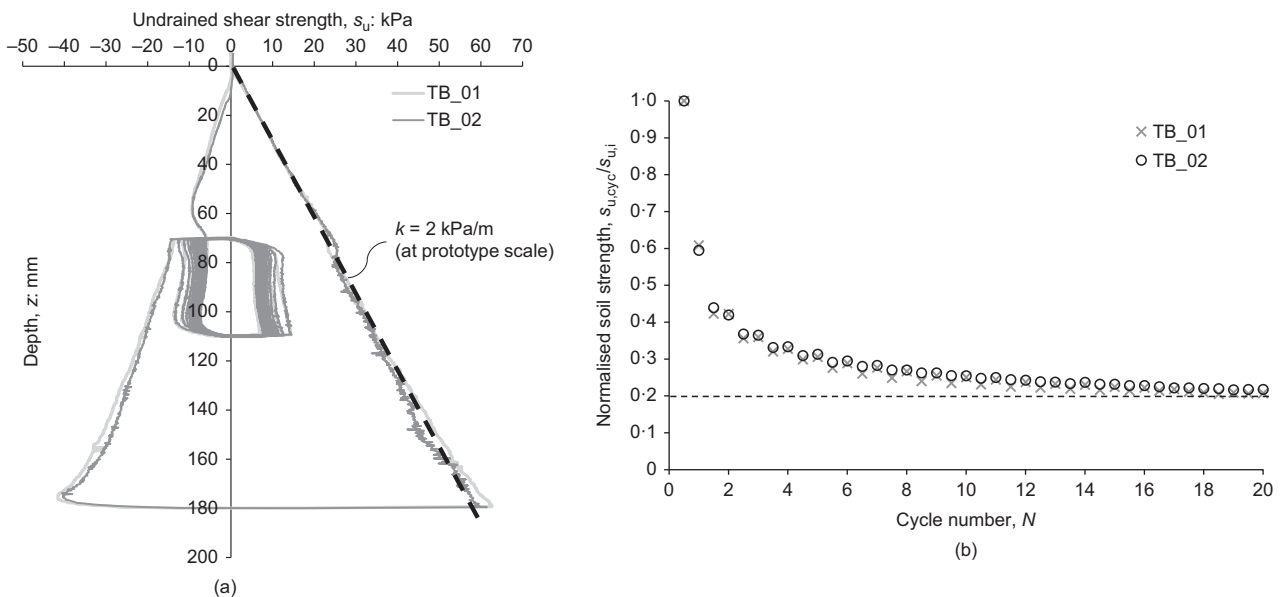


Fig. 3. T-bar test data: (a) undrained shear strength profiles; (b) soil strength variation factor during cyclic remoulding ($z = 75$ mm)

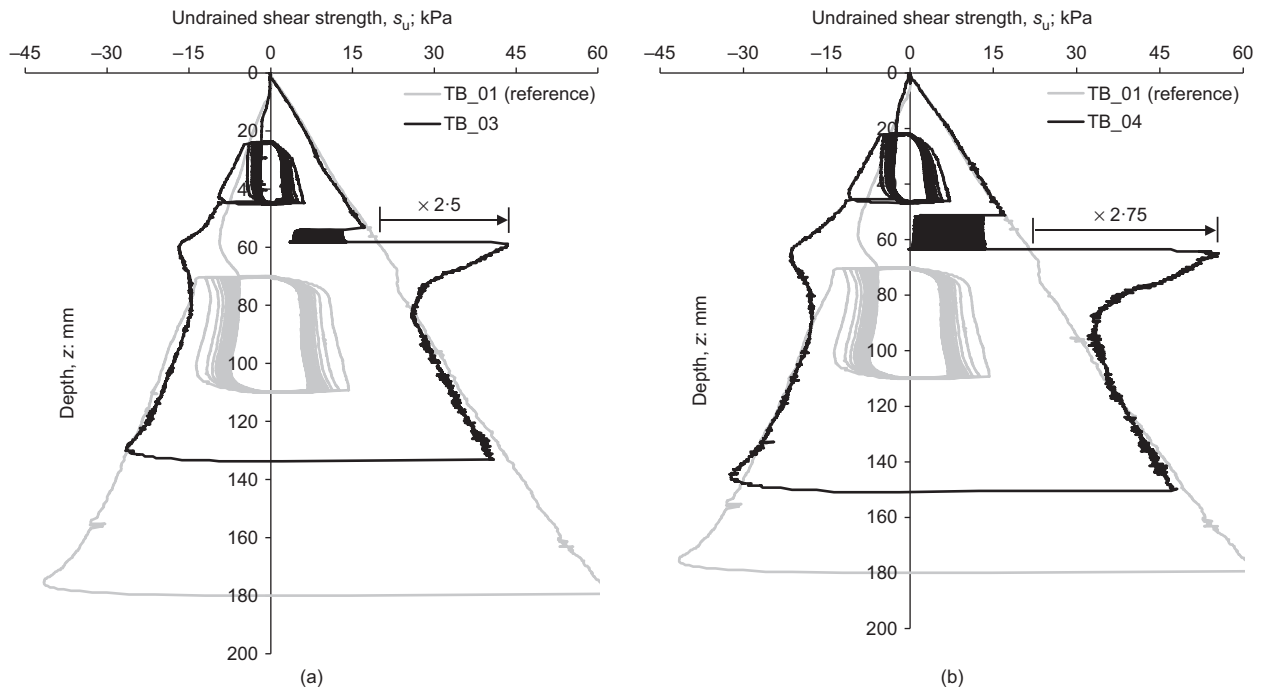


Fig. 4. Undrained shear strength profiles in T-bar tests with load-controlled cycles: (a) TB_03 with 1080 cycles between 0.25 and 0.75 $s_{u,i}$; (b) TB_04 with 1080 cycles between 0 and 0.75 $s_{u,i}$

the excess pore pressure induced by the cyclic loads – which is equally relevant to anchor loading.

Consolidation characteristics. Consolidation coefficients for the carbonate silt were determined from the excess pore pressure dissipation stages of piezocone and piezo-foundation tests conducted at various penetration depths (for the piezocone) and various stress levels (for the piezo-foundation).

In piezocone dissipation tests the pore water flow is primarily radial, controlled by the coefficient of horizontal consolidation, c_h . Dissipations were conducted at depths, $z = 30, 70, 110$ and 150 mm (equivalent to $\sigma'_v \sim 23, 55, 85$ and 117 kPa, respectively) and are shown in Fig. 5 with results in the same soil reported by Chow *et al.* (2019). Excess pore pressure, u_e , is normalised by the initial value, $u_{e,i}$, and plotted against dimensionless time

$$T^* = \frac{c_h t}{R^2 \sqrt{I_r}} \quad (2)$$

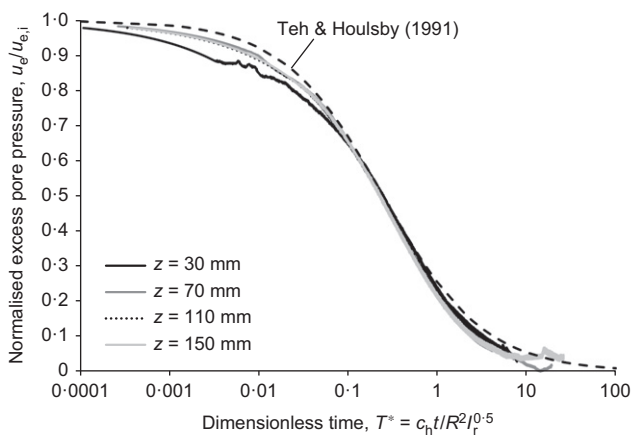


Fig. 5. Excess pore pressure response in piezocone dissipation tests

where R is the piezocone radius = 5 mm, and the rigidity index, $I_r = G/s_u$, uses an elastic shear modulus, G , estimated using (Mahmoodzadeh *et al.*, 2015)

$$G = \frac{3(1-2\nu)}{2(1+\nu)} \frac{p'(1+e)}{\kappa} \quad (3)$$

where ν is Poisson ratio; κ is the slope of the swelling line; p' is the mean effective stress; and e is the void ratio. Equation (3) together with the s_u profiles in Fig. 3 gives $I_r = 110$. Values of c_h were determined by matching T_{50}^* from the experimental dissipation curves with that from the Teh & Houlsby (1991) theoretical solution.

Consolidation around a circular plate anchor involves both radial and vertical drainage, so piezo-foundation tests were undertaken to indicate this ‘operative’ coefficient of consolidation, c_{op} . The rigid circular piezo-foundation had a diameter, $D_f = 40$ mm, and was instrumented with a pore pressure transducer (PPT) in the centre of the underside of the foundation (Cocjin *et al.*, 2014; Colreavy *et al.*, 2016). The piezo-foundation test involved staged loading to $q_{app} = 12$ kPa, 40 kPa, 80 kPa and 160 kPa, with a dissipation stage at each load. The normalised pore pressure, $u_e/u_{e,i}$, measured at $q_{app} = 12, 40, 80$ and 160 kPa, are plotted with dimensionless time, $T = c_{op} t / D_f^2$, in Fig. 6 together with corresponding finite-element solutions for a rigid circular surface foundation (Gourvenec & Randolph, 2010).

The measured coefficients of consolidation, c_h and c_{op} , demonstrate the expected dependence on stress level (Fig. 7) with $c_h/c_{op} \sim 3$ due to the lower stiffness and higher permeability associated with radial flow. A value of $c_{op} = 4$ m²/year is applicable at the anchor test depth and has been used throughout the interpretation.

Anchor test programme

The four anchor tests are summarised in Table 2. Each test involved an initial monotonic phase to measure the ‘undrained–unconsolidated’ anchor capacity, $q_{a,uu}$. Thereafter, the loading sequences employed in each of the

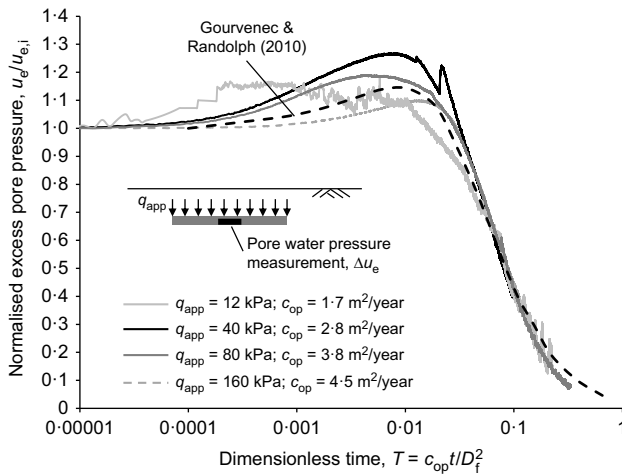


Fig. 6. Excess pore pressure response in piezofoundation dissipation tests

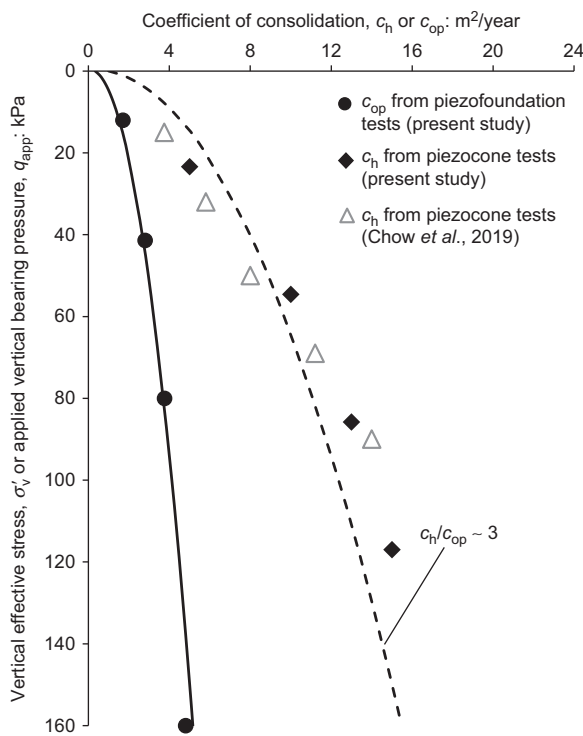


Fig. 7. Coefficients of consolidation from piezocone and piezo-foundation tests

four anchor tests differed as described below and as shown in Fig. 8.

- Test 1 (Fig. 8(a)) involved a consolidation period during which the anchor load was maintained at $0.5q_{a,uu}$ for 3 h.
- Test 2 (Fig. 8(b)) involved a cyclic episode, with the cyclic load varying in the range from $0.25q_{a,uu}$ to $0.75q_{a,uu}$ over 1080 cycles.
- Test 3 (Fig. 8(c)) was a combination of tests 1 and 2, with an initial consolidation period followed by a cyclic episode and a final consolidation period.
- Test 4 (Fig. 8(d)) repeated test 3 five times.

Each test ended with a displacement-controlled monotonic stage (using the same velocity, $v_a = 1$ mm/s as in the initial

monotonic stage) to measure the change in anchor capacity due to the prior loading.

ANCHOR TEST RESULTS

Undrained–unconsolidated anchor capacity

The resistance during the initial monotonic phase is shown in Fig. 9, with anchor resistance expressed as the dimensionless factor

$$N_{c,a} = \frac{q_a}{s_{u,i}} \quad (4)$$

where $s_{u,i}$ is the initial soil strength at the anchor mid-height (i.e. at a depth $z = 150$ mm) and q_a is the anchor resistance (i.e. the measured anchor load divided by $A = \pi D_a^2/4$). Each test showed an initial peak in resistance, reducing to a steady value. The initial peak reflects the localised increase in soil strength due to dissipation of installation-induced excess pore pressure, with anchor capacity stabilising (after a displacement of $x/D_a \sim 1.5$) in the range $N_{c,a} = 10.8$ to 11.5 for the four tests. These values are slightly lower than the exact solution for an infinitesimally thin, deeply embedded plate, which gives $N_{c,a} = 12.42$ for a smooth interface and $N_{c,a} = 13.11$ for a rough interface (Martin & Randolph, 2001), although numerical results in Wang *et al.* (2010) and Wang & O'Loughlin (2014) suggest that these values would be approximately 9% higher for the t/D_a in the centrifuge tests. The seemingly low experimental $N_{c,a}$ values may be due to the choice of T-bar capacity factor used to determine $s_{u,i}$, noting that $(s_u/\sigma'_{v0})_{NC} = 0.32$ from the simple shear tests on the same soil (Chow *et al.*, 2019) would require $s_{u,i}$ on Fig. 3(a) to be $\sim 20\%$ lower. In this case the experimental $N_{c,a}$ values would be higher by the same amount, and in better agreement with numerically determined values. Regardless of the bearing factor, the steady resistance on the T-bar and the plate is very similar, consistent with other studies (e.g. Chung & Randolph, 2004).

Effects of maintained load, cyclic loading and reconsolidation on anchor capacity

The anchor responses during the various loading sequences are shown in Fig. 10 and the time histories of displacement and load are provided in Fig. 11. The resulting capacities are referred to as ‘consolidated–undrained’ ($q_{a,cu}$) for tests involving only maintained load, and ‘cyclic–consolidated–undrained’ ($q_{a,ccu}$) for tests that include cycling and also consolidation (either during the cycling or a separate period of maintained load).

In test 1, a maintained load of $q_a = 0.5q_{a,uu}$ was applied for 3 h, which is equivalent to a dimensionless time factor, $T = tc_{op}/D_a^2 = 1.12$. This is sufficient time for $\sim 95\%$ dissipation of excess pore pressure, as established from pore pressure measurements on a deeply embedded plate in the same soil (Zhou *et al.*, 2019b). The resulting capacity is $q_{a,cu} = 780$ kPa ($q_{a,cu}/s_{u,i} = 17.4$), which is a 51% increase relative to $q_{a,uu} = 516$ kPa (Fig. 10). The anchor displacement during the consolidation phase was $x = 0.1D_a$, and was practically complete after 1.5 h, consistent with the estimated consolidation duration (Fig. 11(a)).

Test 2 showed a similar gain in capacity after the 1080 load cycles (over 40 min), with a capacity of $q_{a,ccu} = 737$ kPa ($q_{a,ccu}/s_{u,i} = 16.4$), which is a 50% increase over $q_{a,uu} = 489$ kPa (Fig. 10). The anchor displacement was more significant ($x = 1.25D_a$), although the position stabilised as consolidation occurred (Fig. 11(b)).

Tests 3 and 4 showed even greater gains in anchor capacity. Test 3 combined the maintained and cyclic loading phases employed in tests 1 and 2, arranged as a 3 h maintained load,

Table 2. Summary of anchor tests: loading sequences, test results and simulation results

Test	Episodic loading regime		Number of episodes	Test results				Simulated peak anchor capacity: kPa	Ratio of simulated to measured capacity
	Maintained load	One-way cyclic loading		Maintained load	Anchor capacity factor, $N_{c,a}$	Final anchor capacity: kPa	Anchor capacity increase		
1	$t_c = 3$ h at $0.5q_{a,uu}$	—	1	—	11.5	$q_{a,cu} = 780$	$q_{a,cu}/q_{a,uu} = 1.51$	$q_{a,cu} = 810$	1.04
2	—	$N = 1080$ cycles $q_a = 0.25q_{a,uu} - 0.75q_{a,uu}$	1	—	10.9	$q_{a,ccu} = 737$	$q_{a,ccu}/q_{a,uu} = 1.50$	$q_{a,ccu} = 821$	1.11
3	$t_c = 3$ h at $0.5q_{a,uu}$	$N = 1080$ cycles $q_a = 0.25q_{a,uu} - 0.75q_{a,uu}$	1	$t_c = 3$ h at $0.5q_{a,uu}$	11.6	$q_{a,ccu} = 990$	$q_{a,ccu}/q_{a,uu} = 1.90$	$q_{a,ccu} = 1063$	1.07
4	$t_c = 3$ h at $0.5q_{a,uu}$	$N = 1080$ cycles $q_a = 0.25q_{a,uu} - 0.75q_{a,uu}$	5	$t_c = 3$ h at $0.5q_{a,uu}$	11.0	$q_{a,ccu} = 1230$	$q_{a,ccu}/q_{a,uu} = 2.50$	$q_{a,ccu} = 1304$	1.06
								Average	1.07

followed by 1080 cycles and a final 3 h maintained load (see Fig. 8(c)). Test 4 involved the same pattern of loading as test 3, but was repeated five times (see Fig. 8(d)).

Test 3 resulted in a capacity of $q_{a,ccu} = 990$ kPa ($q_{a,ccu}/s_{u,i} = 22.2$), which is almost double the undrained unconsolidated capacity, $q_{a,uu} = 521$ kPa ($q_{a,uu}/s_{u,i} = N_{c,a} = 11.6$). In test 4, the five episodes of consolidation and cyclic loading further enhanced the strength gain to $q_{a,ccu} = 1230$ kPa ($q_{a,ccu}/s_{u,i} = 27.5$), which is 2.5 times the initial $q_{a,uu} = 492$ kPa ($q_{a,uu}/s_{u,i} = N_{c,a} = 11$).

The total anchor displacement in test 3 and test 4 was $x \sim 0.1D_a$, with practically all of this displacement occurring during the initial consolidation phase, consistent with test 1. The displacement during subsequent cyclic loading stages was smaller than in test 2 (which had no initial maintained load period) because the cyclic loads were a lower proportion of the current anchor capacity.

The observed gains in anchor capacity due to consolidation under maintained and cyclic loading are consistent with the hardening behaviour in the cyclic (load-controlled) T-bar tests. In both cases, excess pore pressure from continuous one-way cyclic loading or maintained load dissipates, causing a gain in soil strength. The T-bar tests show that a higher load amplitude leads to a higher strength gain (Fig. 4). The anchor tests show that additional cycles lead to higher capacity gains (Fig. 10). Both effects are consistent with the level of pore pressure generation driving the level of subsequent strength gain.

BACK-ANALYSIS USING EFFECTIVE STRESS FRAMEWORK

In this section, the effective stress framework described in Zhou *et al.* (2019a) is applied to simulate the change in anchor capacity due to the load sequences applied. Calculation of anchor capacity, q_a , requires selection of an anchor capacity factor, $N_{c,a}$, and the current undrained shear strength, s_u

$$q_a = N_{c,a}s_u \quad (5)$$

Changes in foundation capacity can be interpreted solely as changes in soil strength, because any changes in the failure mechanism caused by the changing soil strength have minimal influence on the bearing factor $N_{c,a}$ (Stanier & White, 2019). The framework, therefore, focuses solely on the variation in s_u , in order to predict changes in q_a .

Summary of framework

The framework is developed using critical state concepts, and is designed as the simplest basis for capturing changes in strength through a linear profile of soil due to development and subsequent dissipation of excess pore pressure. For the anchor tests, the soil domain is a horizontal row of elements. Vertical effective stress and soil strength is calculated at each soil element throughout the loading sequence (Fig. 12(a)). The framework breaks the event time history into undrained cycles – which generate pore pressure – and consolidation periods – during which pore pressure dissipates.

Example effective stress paths illustrate the framework (Fig. 12(b)). Development of excess pore pressure during undrained shearing leads to a reduction in effective stress at constant specific volume. The maximum excess pore pressure (and hence the lowest effective stress) is associated with fully remoulded conditions, reached at the remoulded state line (RSL, e.g. A–C). This state is reached during the cyclic remoulding phase of TB_01 and TB_02 (Fig. 3(b)). More moderate excess pore pressure generation, such as that developed during the cyclic loading in TB_03 and

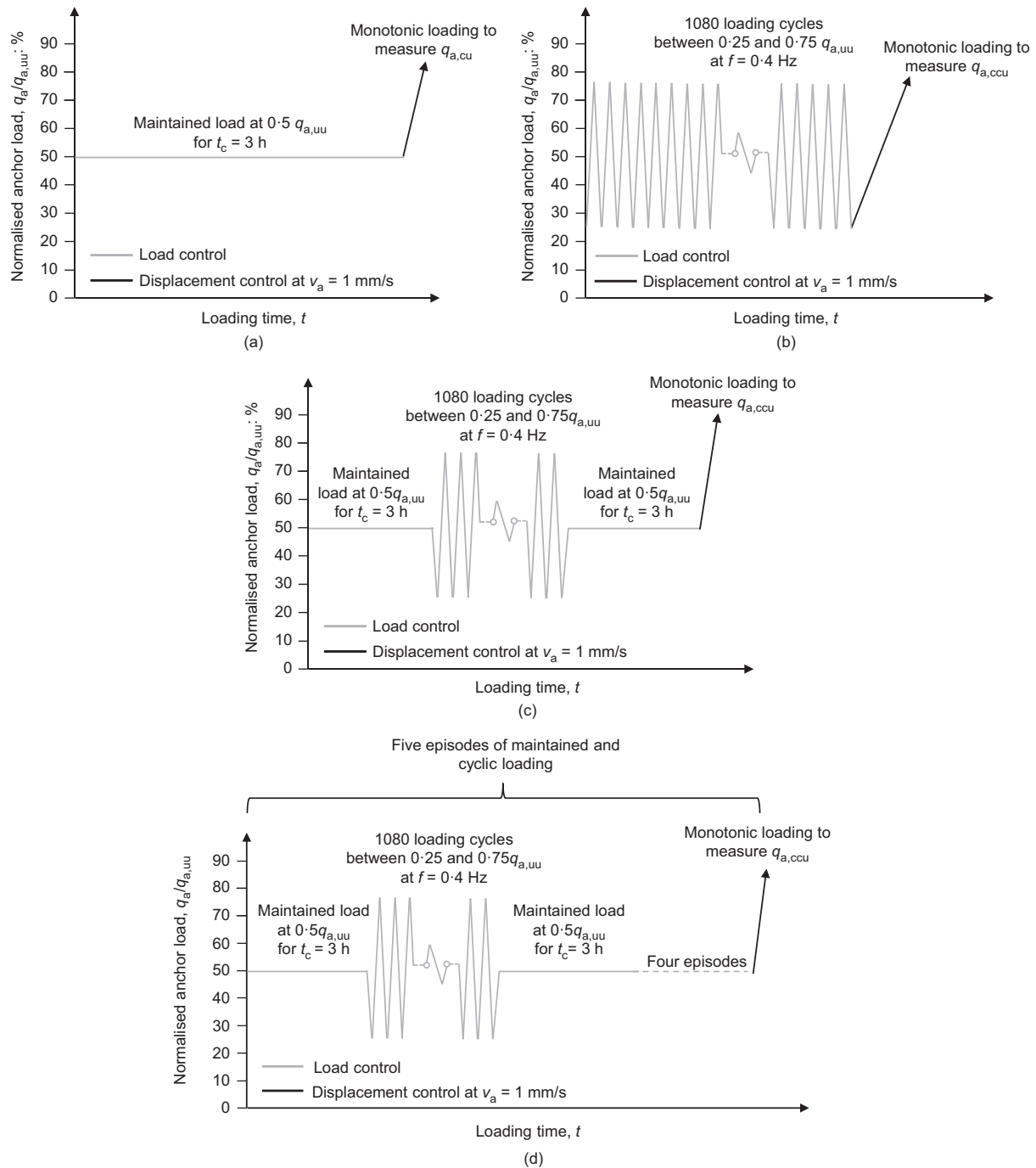


Fig. 8. Loading sequence for anchor tests: (a) test 1; (b) test 2; (c) test 3; (d) test 4

TB₀₄ (Fig. 4), causes a reduction in effective stress to a point between the normal compression line (NCL) and the RSL (e.g. D–E and F–G). During either partial consolidation (path E–F) or full consolidation (path C–D), dissipation of excess pore pressure leads to an increase in effective stress and a reduction in specific volume following the unload–reload line (URL). The effective stress will either return to the initial value (e.g. point D) or potentially to a higher effective stress state if the consolidation phase involves a maintained load (e.g. point I).

The components of the framework analysis as applied to the anchor are summarised below, with further details provided in Zhou *et al.* (2019a).

- (a) Excess pore pressure generation and effective stress. The excess pore pressure, $u_e(\hat{x})$ ($\hat{x} = x/D_a$), is generated at a

rate linked to the shear strain, ε , at each soil element. The rate of excess pore pressure generation is highest at the initial stress state ($\sigma'_{v0} = \gamma'z$ on the NCL for a normally consolidated soil) and close to zero as the vertical effective stress approaches the RSL (from point A–B in Fig. 12(b)) (Zhou *et al.*, 2019a). The vertical effective stress on the RSL, $\sigma'_{v,RSL}$, can be expressed directly in terms of the initial specific volume as

$$\sigma'_{v,RSL}(\hat{x}) = \left(\frac{s_u}{\sigma'_{v0}} \right)_{NC} \frac{\sigma'_{v0}}{\Phi S_t} \exp \left\{ \frac{\Lambda [\Gamma_{NCL} - v_i(\hat{x}) - \lambda \ln(\sigma'_{v0})]}{\lambda - \kappa} \right\} \quad (6)$$

where $(s_u/\sigma'_{v0})_{NC}$ is the normally consolidated undrained strength ratio; Λ is the plastic volumetric strain ratio; Γ_{NCL} is the specific volume at $\sigma'_v = 1$ kPa on the NCL; v_i is the initial specific volume; κ is the gradient of the

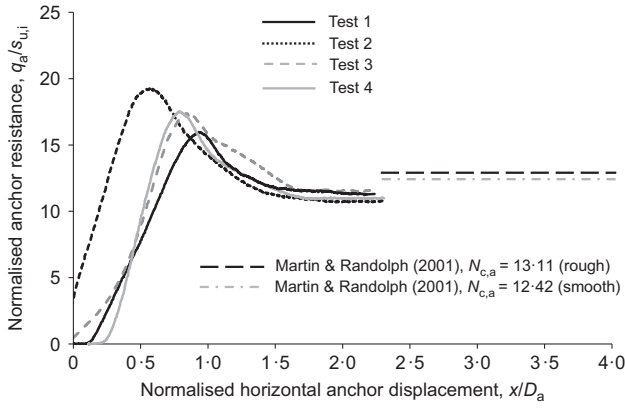


Fig. 9. Anchor capacity response during the initial monotonic loading stage

unloading–reloading line (URL); λ is the gradient of the NCL; S_t is the soil sensitivity; and Φ is a lumped strength parameter.

The excess pore pressure generation rate is

$$\frac{\delta u_e(\hat{x})}{\delta \varepsilon(\hat{x})} = \frac{\chi}{\varepsilon_{98}} \left[\frac{u_{e,r}(\hat{x})}{u_{e,\max}(\hat{x})} \right]^p \quad (7)$$

where

$$\chi = \frac{(1 - 0.01^{1-p})}{1-p} u_{e,\max}(\hat{x}) \quad (8)$$

and ε_{98} is the characteristic shear strain associated with a degree of remoulding equal to 98%; p is a constant power that affects the shape of the pore pressure generation; χ is a characteristic pressure that varies with specific volume, v . The rate is proportional to $u_{e,r}/u_{e,\max}$, which varies from unity down to zero as pore pressure builds up. $u_{e,\max}$ is the maximum pore pressure, given by the difference between the equilibrium stress, $(\sigma'_{v,eqm} = \sigma'_{v0} + \sigma_a)$ and $\sigma'_{v,RSL}$, while $u_{e,r}$ is the remaining potential excess pore pressure, $(\sigma'_v - \sigma'_{v,RSL})$ (distance B–C on Fig. 12(b)). The incremental (absolute) shear strain is calculated as the anchor moves horizontally

with a given displacement, $\delta \hat{x}$, and weighted by the strain influence function, $\mu(\hat{x})$, with boundaries that extend a normalised distance β ahead and behind the anchor (Zhou *et al.*, 2019a). Any maintained load on the anchor generates additional stress that is added to the vertical self-weight stress to enhance the equilibrium effective stress in the ground. This extra stress, at position δ relative to the anchor, is $\sigma_a = I_\sigma(\delta) K_0 q_a$ where $I_\sigma(\delta)$ is the influence factor describing the stress distribution away from the anchor following Boussinesq (1885) and Poulos & Davis (1974); K_0 is a lateral earth pressure coefficient; and q_a is the maintained load.

- (b) Consolidation process. Dissipation of excess pore pressure during consolidation is described by a simple hyperbolic model (Chatterjee *et al.*, 2013; Zhou *et al.*, 2019a), which is expressed in rate form as

$$\frac{\delta u_e(\hat{x})}{\delta t} = - \frac{u_{e,i}(\hat{x}, t) c_{op}^m t^{m-1} (D_a^2 T_{50})^m m}{[(D_a^2 T_{50})^m + (c_{op} t)^m]^2} \quad (9)$$

where t is the period of (consolidation) time; c_{op} is the operative coefficient of consolidation; m is a constant that controls the shape of the dissipation response; and T_{50} is the dimensionless time factor for 50% dissipation of the initial excess pore pressure.

- (c) Soil strength response. The current undrained shear strength at each soil element is calculated from the vertical effective stress, $\sigma'_v(\hat{x})$, by way of a lumped strength parameter, Φ

$$s_u(\hat{x}) = \Phi \sigma'_v(\hat{x}) \quad (10)$$

An average undrained shear strength mobilised by the anchor, $s_{u,av}$, is obtained by integrating the undrained shear strength within an influence zone (described by $v_s(\hat{x})$) with a triangular weighting function extending a distance, α , behind and in front of the anchor

$$s_{u,av} = \int_{\hat{x}_m - \alpha}^{\hat{x}_m + \alpha} s_u(\hat{x}) v_s(\hat{x}) dx \quad (11)$$

Prior to failure, a proportion of the strength, $s_{u,mob}$, is progressively mobilised with a changing tangent stiffness,

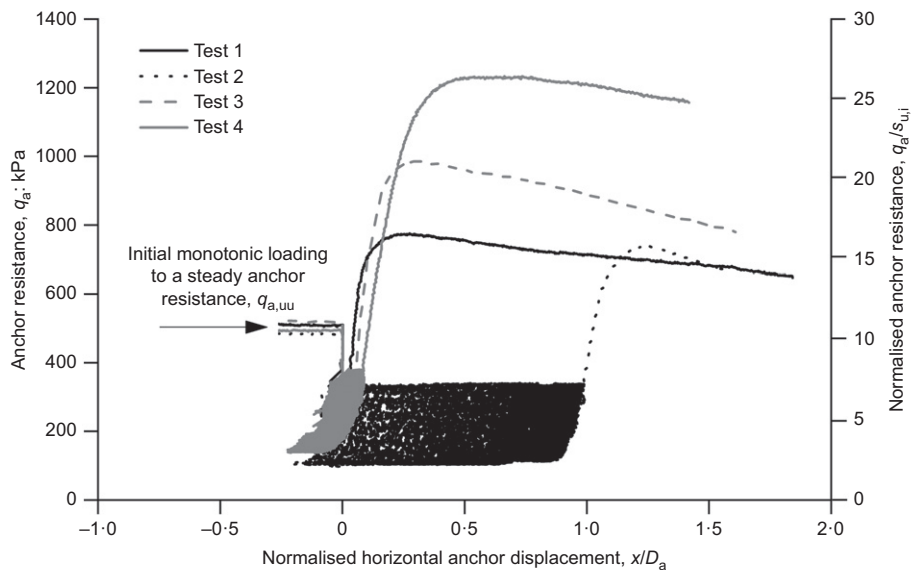


Fig. 10. Increase in anchor resistance due to consolidation during (and following) maintained and cyclic loading

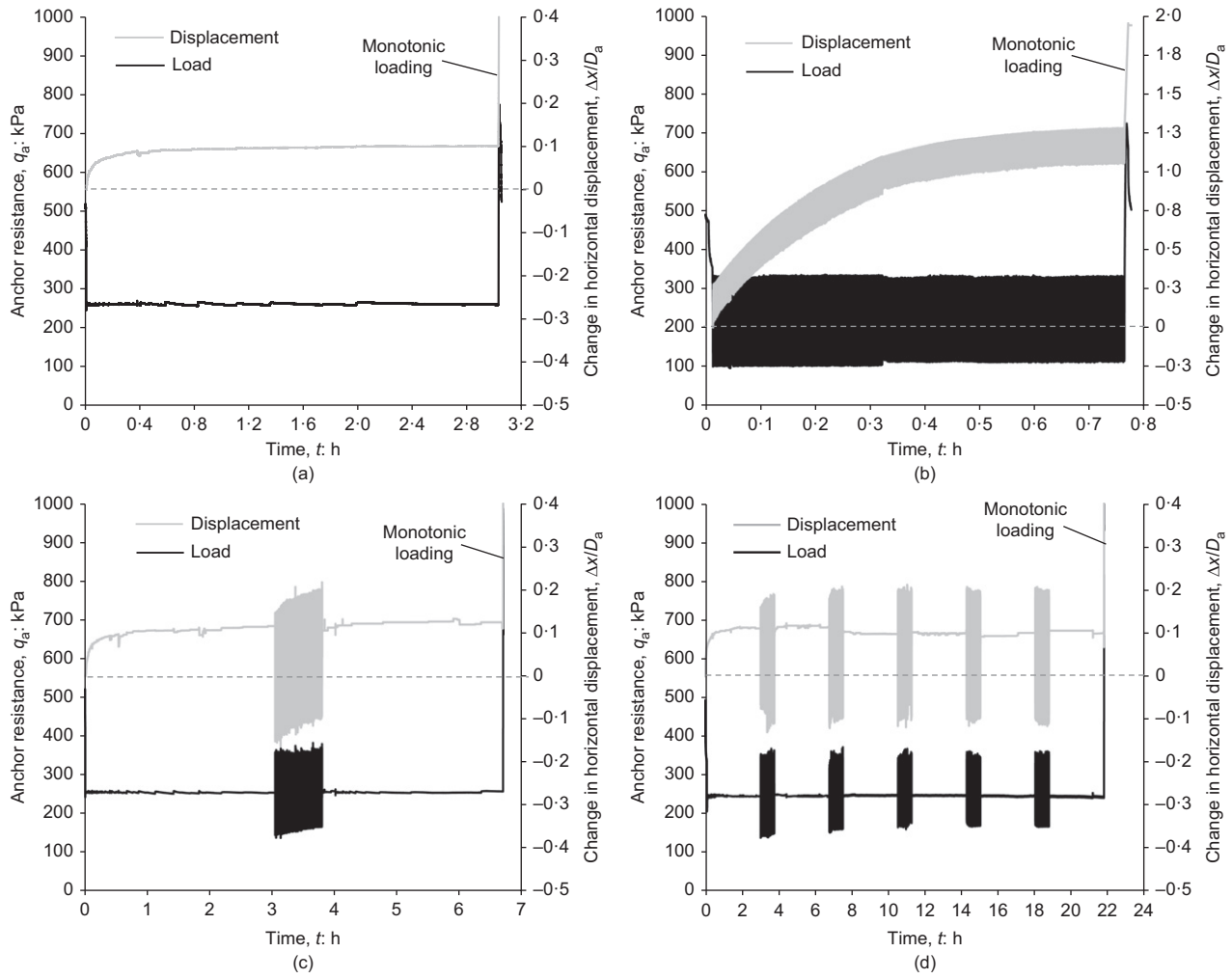


Fig. 11. Maintained and cyclic loading sequence and the corresponding anchor displacement response: (a) test 1; (b) test 2; (c) test 3; (d) test 4

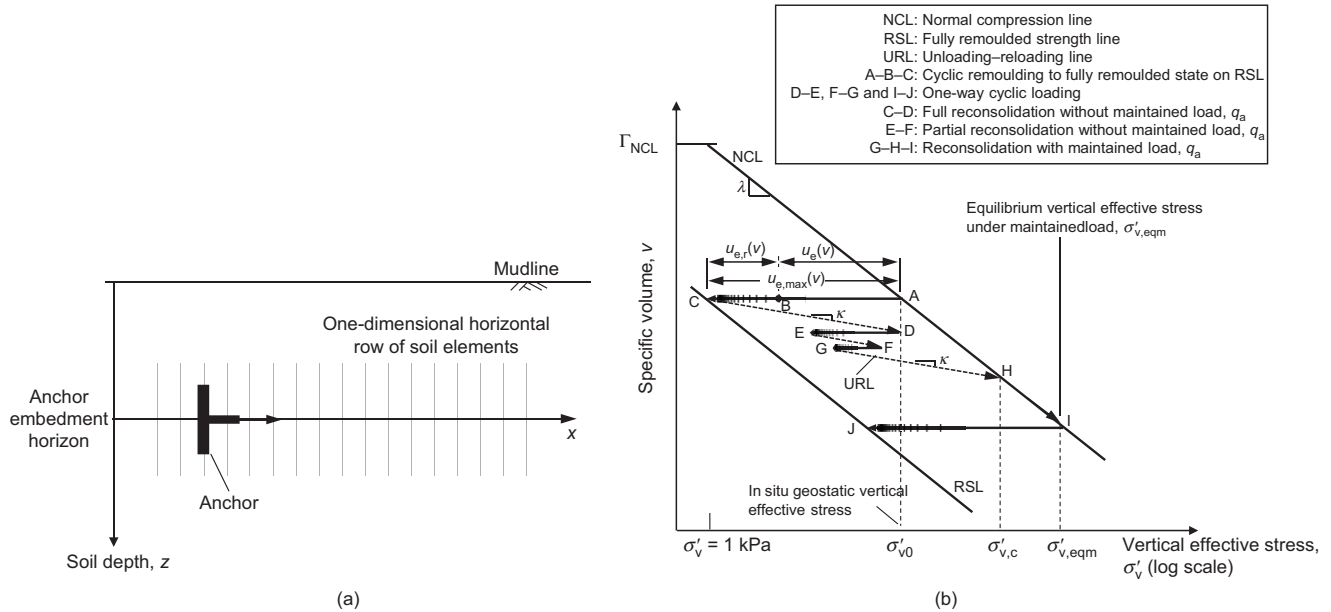


Fig. 12. Effective stress framework: (a) one-dimensional horizontal row of soil elements for this study; (b) effective stress paths due to remoulding, cyclic loading, reconsolidation and maintained load expressed as

where

$$\delta \left(\frac{s_{u,mob}}{s_{u,av}} \right) = \delta(\hat{x}) K \quad (12) \quad K = \left\{ 1 - \left[\frac{\Delta(s_{u,mob}/s_{u,av})}{\Delta(s_{u,max}/s_{u,av})} \right]^\zeta \right\} K_{max} \quad (13)$$

in which ζ is the power law parameter to account for the nonlinear change in tangent stiffness; $(s_{u,max}/s_{u,av})$ is the potential change after any reversal; the effective tangent stiffness, K , varies non-linearly from a maximum stiffness, K_{max} to 0 at $s_{u,mob}/s_{u,av} = 1$ (see Zhou *et al.* (2019a) for further details).

Selection of framework parameters

The model parameters used in the simulations are summarised in Table 3. Many parameters are directly defined in the experiments – for example, the anchor diameter, effective soil unit weight, overconsolidation ratio and soil sensitivity. The critical state soil parameters (κ , λ and Γ_{NCL}) are established from oedometer tests (Table 1) and the normally consolidated undrained shear strength ratio $(s_u/\sigma'_{v0})_{NC}$ from the initial penetration of a T-bar test.

The excess pore pressure generation parameters (ε_{98} , p and β) were obtained by fitting to the cyclic T-bar results shown in Fig. 3. Excess pore pressure dissipation parameters, T_{50} and m , were taken from previous back-analyses of a circular plate at a normalised depth, $z/D_a = 3.5$ in the same soil (Zhou *et al.*, 2019b). This requires selection of an 'operative' coefficient of consolidation, c_{op} , as $T_{50} = t_{50}c_{op}/D_a^2$ (where t_{50} is actual, rather than dimensionless time). Fig. 7 indicates $c_{op} = 4 \text{ m}^2/\text{year}$ (Fig. 7) for this soil and anchor geometry. For field applications, c_{op} may be selected as an average of c_v from Rowe cell (or oedometer) tests and c_h from a piezocene or piezoball test.

The final group of parameters in Table 3 controls the strength and stiffness mobilisation response. The lumped strength parameter was taken as $\Phi = 1.62$, selected by scaling $(s_u/\sigma'_{v0})_{NC}$ by the ratio of the drained to undrained T-bar penetration resistance (4.2 for this soil, from Chow *et al.* (2019)). The extent of the strength influence zone was taken as $\alpha = 0.5$ (i.e. $0.5D_a$), consistent with the size of the failure mechanism for a deeply buried plate (e.g. Yu *et al.*, 2011; Wang & O'Loughlin, 2014), and equal to the value in previous analyses of spudcan penetration (Zhou *et al.*, 2019a). For the simulation of the episodic T-bar test, a value of $\alpha = 1$ was selected, meaning that the operative strength was calculated over a zone that extended by one bar diameter away from the centreline, matching the size of numerically observed failure mechanisms (Einav & Randolph, 2005; Zhou *et al.*, 2019a).

The maximum stiffness, K_{max} , and its decay parameter, ζ , were taken as 210 and 4.55, respectively, based on a best fit to

the cyclic phase of test 2. These final two parameters were the only ones fitted directly to the anchor test results. All other parameters have been sourced from the T-bar results, theoretical considerations, or other previously published tests.

Results of T-bar test simulations

The framework performance is first demonstrated by way of simulations of an episodic T-bar test that was performed in the same sample as the anchor tests following the protocol set out by Hodder *et al.* (2009). This type of test involves undrained penetration (at $v_p = 3 \text{ mm/s}$) to a depth, $z = 75 \text{ mm}$, followed by three episodes of 20 displacement-controlled cycles over $z = 30$ to 75 mm , after which the T-bar was maintained at the base of the cycles for a period of 1 h.

The simulation used the parameters set out in Table 3 and the full procedures are described in Zhou *et al.* (2019a), who report equivalent tests and simulations in kaolin clay.

The simulated and measured profiles of penetration resistance are compared in Fig. 13(a), with the mid-cycles values of $s_u/s_{u,i}$ highlighted in Fig. 13(b). The degradation and recovery of strength are both well captured and the strength at the start of the third episode has nearly recovered to the initial value.

Results of anchor test simulations

The anchor capacity is the product of a bearing factor and an average undrained strength around the anchor. Specific bearing factors were taken for each test ($N_{c,a} = 11.5, 10.9, 11.6$ and 11 for tests 1, 2, 3 and 4) based on the initial monotonic loading stage (Table 2). These values were used in the simulations of each test to separate out these minor test-to-test variations in anchor capacity from the changes in capacity within each test.

The framework, using the parameters listed in Table 4, was then employed to calculate the operative soil strength and therefore the anchor resistance throughout each test.

Changes in anchor capacity. Figure 14 compares the simulated and measured evolution of anchor capacity for each test. Overall the simulations provide good agreement with the measurements, with the peak resistance predicted to within 7% on average (Table 2). There is a tendency to underestimate the post-peak resistance, which is perhaps

Table 3. Summary of framework parameters used in the simulation of the episodic cyclic T-bar test

Framework component	Parameter	Description	Value
Geometry	D	Diameter of the anchor	0.75 m (prototype scale)
Soil characteristics	γ'	Effective unit weight	5.2 kN/m ³
	OCR	Overconsolidation ratio	1
	$S_{t,cyc}$	Soil sensitivity	5
Critical state model	λ	Compression index	0.287
	κ	Swelling index	0.036
	$(s_u/\sigma'_{v0})_{NC}$	Normally consolidated undrained strength ratio	0.385
	Γ_{NCL}	Specific volume, v , at $\sigma'_v = 1 \text{ kPa}$ on NCL	4
Excess pore pressure generation	ε_{98}	Cumulative shear strain parameter	100
	p	Shear strain rate parameter	2.9
	β	Strain influence zone extent	1D
Consolidation process	T_{50}	Non-dimensional time for 50% consolidation	0.09
	m	Embedment level parameter	1.05
General soil strength and stiffness response	Φ	Lumped strength parameter	1.62
	α	Strength influence zone extent	1D
	K_{max}	Maximum tangent stiffness	32.5
	ζ	Power law parameter for strength mobilisation	0.32

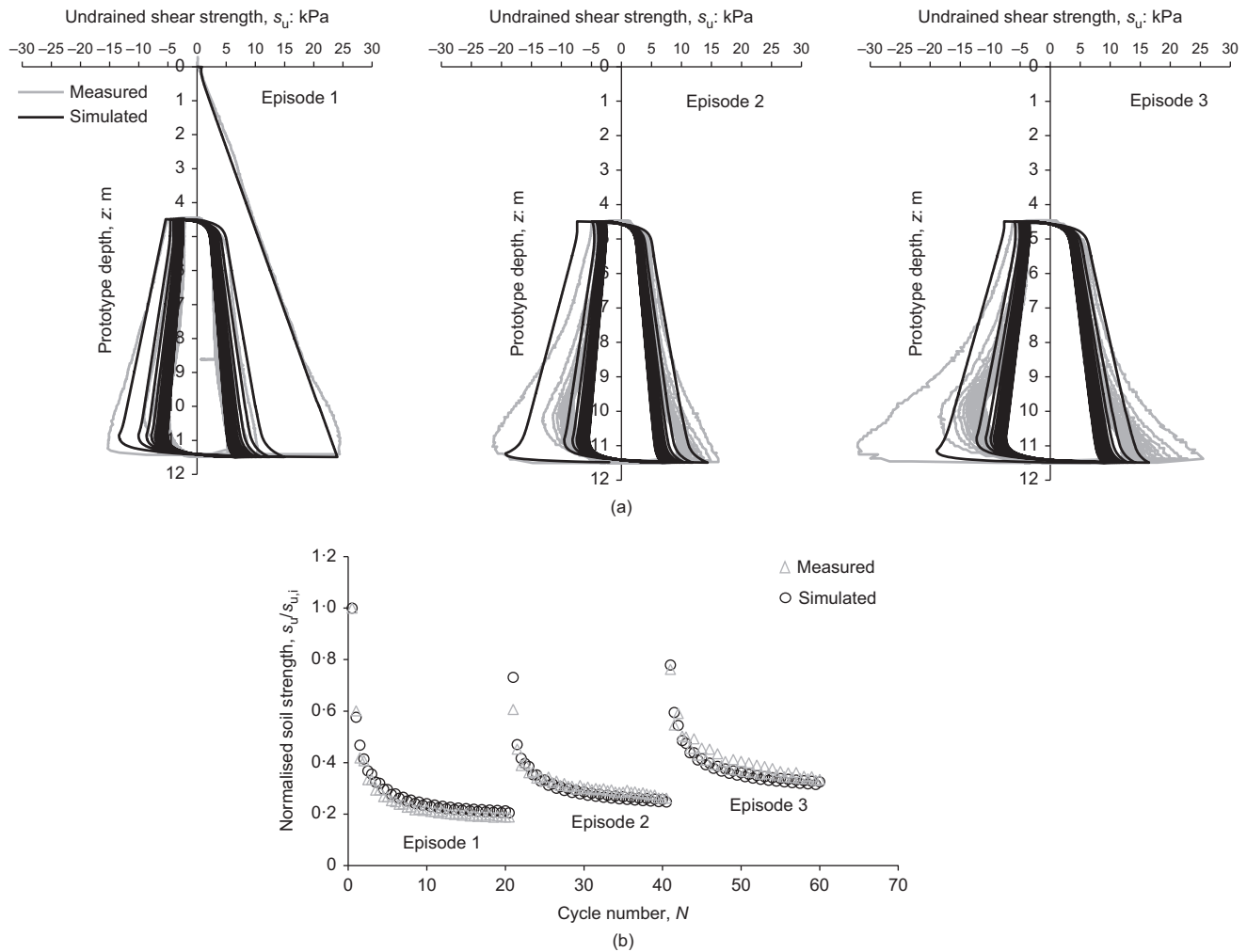


Fig. 13. Comparison of experimental and simulated episodic cyclic T-bar: (a) depth profiles of undrained shear strength; (b) evolution of normalised soil strength, $s_u/s_{u,i}$, during and after cycles at the mid-depth of the cycles

because the model does not capture the strengthened soil being moved forward with the anchor.

An additional simulation was undertaken to illustrate the limiting peak anchor capacity by extending test 4 to 200 episodes of cyclic loading and reconsolidation. By the end of this simulation, the capacity reached $q_{a,ccu} = 2070$ kPa, which is >4 times more than the initial $q_{a,uu}$. This example illustrates the potential for even greater gains in anchor capacity than were observed in the relatively short-term centrifuge model tests.

This additional simulation illustrates the potential for the model to be used to maintain an updated value of the anchor capacity, in response to the whole-life loading it has experienced. The movements of a floating facility are commonly monitored and used to estimate loading and fatigue within the facility and its mooring system (e.g. Renzi *et al.*, 2017). Similarly, the motions or mooring loads could be fed into this anchor model, in order to maintain a continuously updated estimate of the changing capacity. The model then becomes a digital twin of the anchor, to support integrity management, design condition updating and life extensions.

Variation in effective stress and voids ratio. Figure 15 shows the variation in effective stress and specific volume calculated by the framework for soil elements at various locations relative to the anchor, which are indicated in Fig. 14 for each

test. Some observations from these stress paths are listed below.

- Test 1 (Fig. 15(a)). Effective stress paths are provided for soil elements at two locations; $x/D_a = 0$, in front of the plate at the end of the initial monotonic stage, and $x/D_a = 0.26$, which is where the peak anchor capacity is mobilised during the post-consolidation monotonic stage. During the initial monotonic loading phase, excess pore pressure develops, reducing σ'_v from point A' to point B' (at $x/D_a = 0$) and point B (at $x/D_a = 0.26$). The vertical effective stress at point B is higher than at point B' as this soil element is initially further from the anchor. During the consolidation phase the effective stress path follows the URL (B–C or B'–C') and then the NCL to point D or D'.
- The final monotonic stage causes excess pore pressures to redevelop, such that σ'_v reduces to points E' and E for $x/D_a = 0$ and $x/D_a = 0.26$, respectively. Points B' (at $x/D_a = 0$) and E (at $x/D_a = 0.26$) represent the difference in stress state between the initial and final monotonic stages. As the effective stress at point E is higher than at point B', the soil strength, and hence the anchor capacity, is higher.
- Test 2 (Fig. 15(b)). Three soil elements are shown for this test, due to the high horizontal displacement: $x/D_a = 0$, 0.45 and 1.2. The response at $x/D_a = 0$ matches test 1 (Fig. 15(a)), with σ'_v reducing from A'' to

Table 4. Summary of framework parameters used in the simulation of the anchor tests

Framework component	Parameter	Description	Value	Remarks
Geometry	D	Anchor diameter (prototype scale)	5.25 m	—
Soil characteristics	γ'	Effective unit weight	5.2 kN/m ³	—
	OCR	Overconsolidation ratio	1	Normally consolidated soil sample for this study
	$S_{t,cyc}$	Soil sensitivity	5	Measured by cyclic T-bar test
	c_{op}	Coefficient of consolidation	4 m ² /year	Measured by piezo-foundation test
Critical state model	λ	Compression index	0.287	λ defines the gradient of NCL
	κ	Swelling index	0.036	κ defines the gradient of URL
	$(s_u/\sigma'_{v0})_{NC}$	Normally consolidated undrained strength ratio	0.385	Based on an undrained shear strength gradient, $k = 2$ kPa/m and effective unit weight, $\gamma' = 5.2$ kN/m ³
Excess pore pressure generation	Γ_{NCL}	Specific volume, v , at $\sigma'_v = 1$ kPa on NCL	4	Measurements from Chow <i>et al.</i> (2019) and Zhou <i>et al.</i> (2019b)
	ε_{98}	Cumulative shear strain parameter	100	ε_{98} and p for excess pore pressure generation in equation (7)
	p	Shear strain rate parameter	2.9	
	β	Strain influence zone extent	0.5D	Selected to define the shear strain influence zone, as informed by clay failure mechanisms (e.g. Yu <i>et al.</i> , 2011).
Consolidation process	T_{50}	Non-dimensional time for 50% consolidation	0.07	T_{50} and m for excess pore pressure dissipation via equation (9)
	m	Embedment level parameter	0.92	
General soil strength and stiffness response	Φ	Lumped strength parameter	1.62	Used to calculate the undrained shear strength from the current vertical effective stress by way of equation (10)
	α	Strength influence zone extent	0.5D	Selected to define the strength influence zone, as informed by clay failure mechanisms (e.g. Yu <i>et al.</i> , 2011)
	K_{max}	Maximum tangent stiffness	210	Used to calculate effective tangent stiffness during soil strength mobilisation
	ζ	Power law parameter for strength mobilisation	4.55	by way of equation (12)

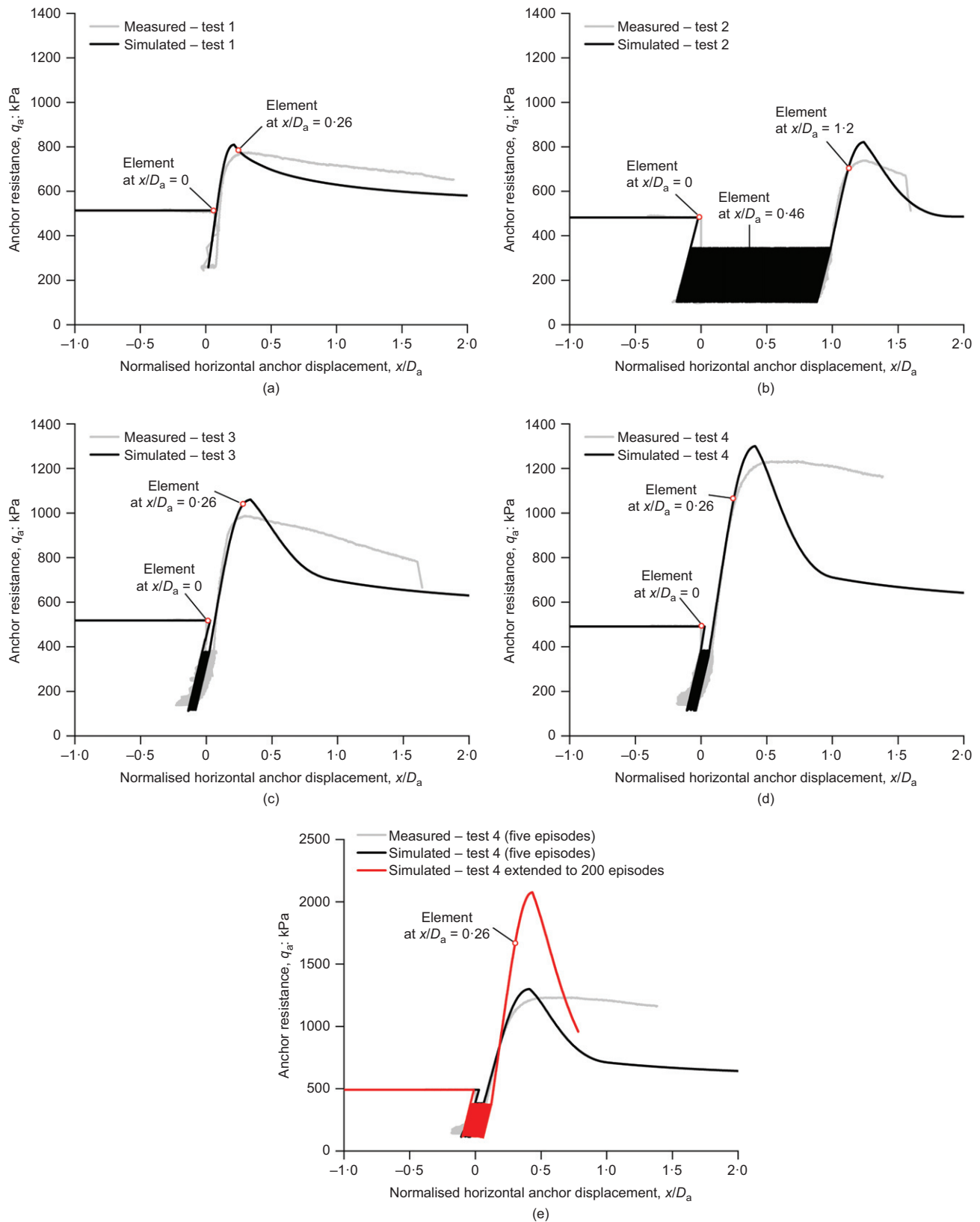


Fig. 14. Experimental and simulated anchor capacities: (a) test 1; (b) test 2; (c) test 3; (d) test 4; (e) test 4 extended to 200 episodes

B". The effective stress at $x/D_a = 0.45$ reduces very slightly from A' to B', being at the edge of the strain influence zone. The stress at $x/D_a = 1.2$ is unaffected, being outside the strain influence zone during this stage.

- (d) During cyclic loading the soil elements respond according to their location relative to that of the plate.

The effective stress initially reduces at $x/D_a = 0$, but then begins to increase (at $N = 35$) as excess pore pressure dissipation outweighs the continuing generation. After 170 cycles $x/D_a = 0$ is outside the strain influence zone, so only dissipation occurs thereafter, following the URL to point C". At $x/D_a = 0.45$ the modest pore pressure from the initial monotonic stage (point B') is

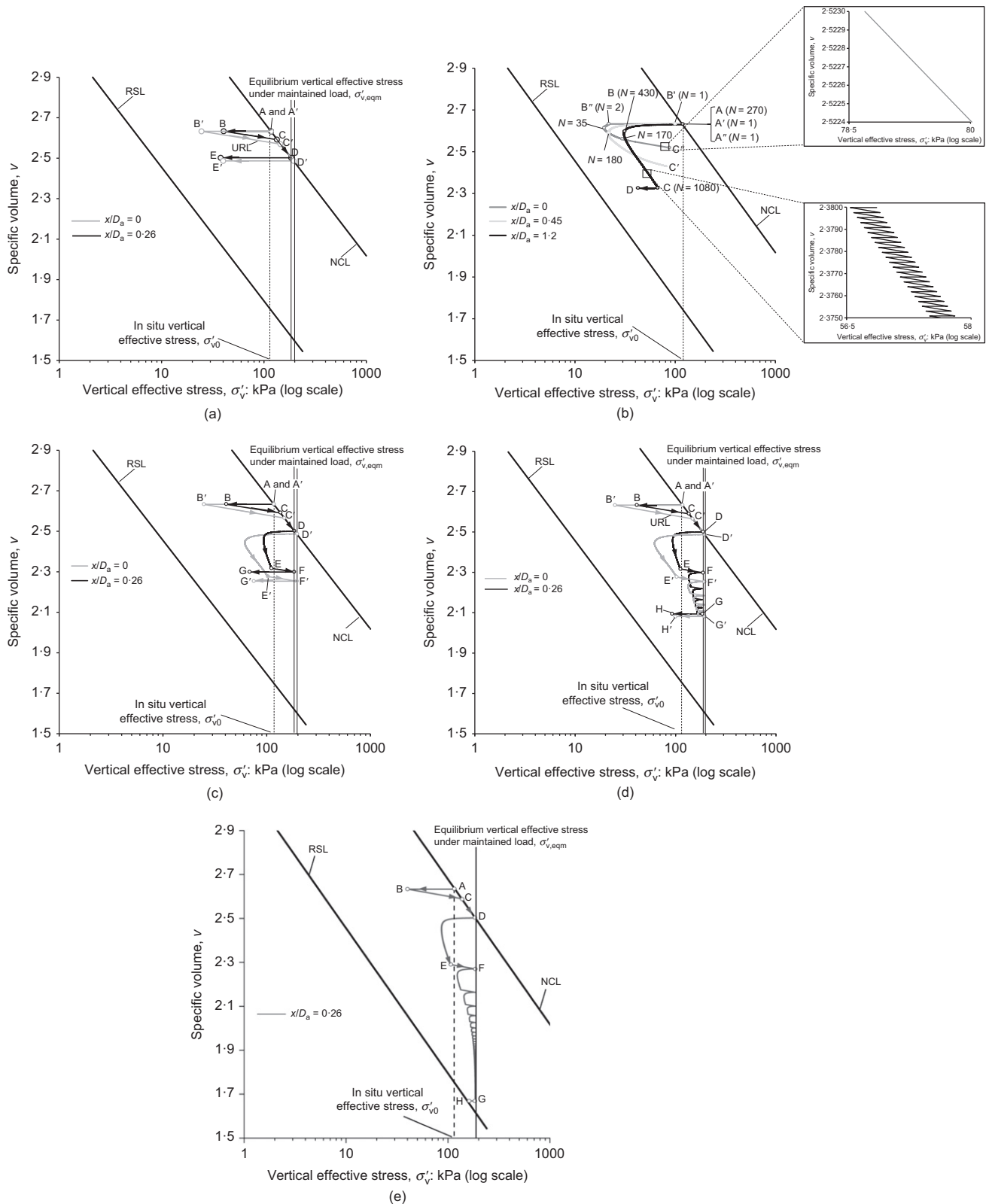


Fig. 15. Effective stress paths: (a) at $z/D_a = 0$ and 0.26 for test 1; (b) at $z/D_a = 0, 0.46$ and 1.2 for test 2; (c) at $z/D_a = 0$ and 0.26 for test 3; (d) at $z/D_a = 0$ and 0.26 for test 4; (e) at $z/D_a = 0.26$ for an extended simulation of test 4 (involving 200 episodes)

followed by significant additional pore pressure generation during the initial cycles. However, after $N = 180$ σ'_v starts to increase with the pore pressure dissipation outweighing pore pressure generation. By $N = 1080$, $x/D_a = 0.45$ is almost outside the strain influence zone, so the stress path is dominated by dissipation towards C' . The soil element at $x/D_a = 1.2$

only enters the strain influence zone at $N = 270$, and σ'_v initially reduces until $N = 430$. Thereafter, the stress increases to point C following a path that is approximately parallel to the NCL and RSL.

(e) During the final monotonic stage the soil elements at $z/D_a = 0$ and 0.45 do not respond as they are not within the strain influence zone, whereas at $z/D_a = 1.2$, σ'_v

reduces to point D, at a higher vertical effective stress than at point B and consequently a higher soil strength.

- (f) Test 3 (Fig. 15(c)). Effective stress paths at $x/D_a = 0$ and 0.26 are shown, consistent with test 1. The responses at $x/D_a = 0$ and 0.26 for the initial monotonic stage and the maintained load stage (to D' and D) match test 1. As in test 2, cyclic loading causes an initial reduction and then increase in effective stress, with both soil elements responding to the cycle-by-cycle change in pore pressure over the complete 1080 cycles. The plate movement in this test is significantly reduced relative to test 2 because of the consolidation during the initial maintained load stage. The magnitude of pore pressure at each soil element depends on their location relative to the plate. The effective stress path for the final maintained load stage of the test follows the URL along E'-F' ($x/D_a = 0$) and E-F ($x/D_a = 0.26$), reaching slightly different limiting effective stresses (F' and F) due to the different (horizontal) position of each element relative to the anchor, and therefore different values of $\sigma'_{v,eqm}$.
- (g) The final monotonic stage of the test causes a reduction in σ'_v to point G' or point G, which are higher than at point B', yielding a gain in anchor capacity.
- (h) Test 4 (Figs 15(d) and 15(e) – extended). As for test 3, soil elements at $x/D_a = 0$ and 0.26 are shown. The initial response matches test 3, and then continues by repeating the episodes of cyclic loading and maintained load. Progressively less excess pore pressure is generated, such that the eventual effective stress state (point H for $x/D_a = 0.26$) is at a high effective stress and hence soil strength. An extended simulation of the same test involving 200 episodes of cyclic and maintained load (Fig. 15(e)) illustrates the progressive decay in excess pore pressure generation as $u_{e,max}$ reduces from ~179 kPa in the first episode to ~19 kPa in the final episode. The limiting soil strength is at $\sigma'_{v,eqm}$ on the RSL, which corresponds to a soil strength that is 6.9 times the initial undrained soil strength (point B). This ratio exceeds the ratio of drained to undrained penetration resistance for this soil ($\Phi/(s_u/\sigma'_v)_{NC} = 4.2$) due to the additional effective stress created by the maintained load ($\sigma'_{v,eqm} - \sigma'_{v0}$).

Overall, the stress paths show that the framework can capture a range of effects that lie behind the observed changes in soil strength and anchor capacity. For example, the level of pore pressure generation depends on the current pore pressure and the loading amplitude, which varies due to the level of anchor load as well as the position relative to the anchor. Also, the progressive consolidation, both during cycles and under maintained load, is illustrated, alongside the resulting changes in anchor capacity.

CONCLUSIONS

Plate anchors offer an efficient solution for mooring floating facilities. This paper describes a set of centrifuge experiments that illustrate how the capacity of a plate anchor in a fine-grained soil increases due to combinations of maintained and cyclic load. The tests show a 50% gain in capacity after full consolidation under a maintained load of 50% of the monotonic undrained capacity. Also, 1080 cycles of one-way undrained cyclic loading over a much shorter period give a similar gain. Combinations of maintained and cyclic loading lead to even higher capacity increases, to ~2.5 times the initial value.

These results are replicated by simulations using the Zhou *et al.* (2019a) effective stress framework. This approach calculates changes in soil strength due to undrained shearing and consolidation and provides insights into the underlying stress paths within the loaded soil. Many of the framework parameters are derived from full-flow penetrometer tests, so there is the potential to bridge from in situ tests to plate anchor design calculations. The prediction approach outlined here is an effective means of establishing the magnitude and timescale of the capacity changes for particular combinations of anchor geometry, loading and seabed properties.

In summary, this paper indicates that a less conservative basis for plate anchor design may be warranted, particularly if loading events are predictable – which is the case, for example, with offloading events for a taut moored floater. Further evidence for more general loading conditions (including an inclined plate and inclined loading) would provide wider validation in this regard. The model shown in this paper can be used to determine how gains in strength raise the reliability of the system, allowing resistance factors to be adjusted accordingly.

The model can also be a 'digital twin' of an anchor, since it can capture the changing capacity in response to any arbitrary loading sequence that the anchor is subjected to. In this way, the model could form part of an asset management system to monitor the integrity of the anchor and its ability to sustain additional loads as a result of revised design conditions or life extension requirements.

ACKNOWLEDGEMENTS

The first author acknowledges his research studentship support from the ARC Industrial Transformation Research Hub for Offshore Floating Facilities and the University of Western Australia. This work was supported by the ARC Industrial Transformation Research Hub for Offshore Floating Facilities, which is funded by the Australia Research Council, Woodside Energy, Shell, Bureau Veritas and Lloyds Register (grant no. IH140100012). The third author acknowledges the support of the Shell Chair in Offshore Engineering at UWA.

NOTATION

b	peak strength parameter, $k_\Phi(\dot{\epsilon}) = \text{OCR}(\dot{\epsilon})^b$
c_h	coefficient of horizontal consolidation
c_{op}	operative coefficient of consolidation
c_v	coefficient of consolidation
D_a	diameter of circular plate anchor
D_f	diameter of piezofoundation
d	diameter of T-bar penetrometer
G	elastic shear modulus
I_r	rigidity index
I_σ	Boussinesq influence factor
K	tangent stiffness
K_{max}	maximum tangent stiffness adopted since the last reversal in penetration or extraction
K_0	lateral earth pressure coefficient
k	soil strength gradient
m	parameter for dissipation rate
$N_{c,a}$	anchor dimensionless factor
p	parameter for pore pressure generation rate
p'	mean effective stress
q_a	anchor resistance
$q_{a,ccu}$	cyclic (or cyclic consolidated) undrained anchor resistance
$q_{a,cu}$	consolidated undrained anchor resistance
q_{app}	applied vertical bearing pressure
$q_{a,uu}$	undrained unconsolidated anchor resistance
S_t	soil sensitivity
s_u	undrained shear strength

$s_{u,av}$	average undrained shear strength
$s_{u,c}$	consolidated soil strength
$s_{u,cyc}$	cyclic undrained shear strength
$s_{u,i}$	initial undrained shear strength
$s_{u,mob}$	mobilised soil strength
$(s_u/\sigma'_{v0})_{NC}$	normally consolidated undrained strength ratio
T	dimensionless time, $T = c_{opt}/D_f^2$
T^*	dimensionless time for piezocone test, $T^* = c_h t/R^2 I_r^2$
T_{50}	dimensionless time required for 50% dissipation of the initial excess pore pressure
t	time
t_{50}	time required for 50% dissipation of the initial excess pore pressure
t_a	thickness of plate anchor
t_c	reconsolidation period
u_e	excess pore pressure
$u_{e,max}$	maximum excess pore pressure
$u_{e,r}$	remaining potential excess pore pressure
v	specific volume
v_a	anchor velocity
v_i	initial specific volume
v_p	penetration velocity
v_s	strength influence function
x	horizontal displacement
z	soil depth
\hat{z}	normalised soil depth, z/D_a
z_m	depth of centre of plate anchor below soil surface
\hat{z}_m	normalised depth, z_m/D_a
α	strength influence zone extent
β	strain influence zone extent
Γ_{NCL}	specific volume, v , $\sigma'_v = 1$ kPa on the normal consolidation line (NCL)
γ'	soil effective unit weight
ε	cumulative (absolute) shear strain
ε_{98}	cumulative (absolute) shear strain required for a degree of remoulding equal to 98%
ζ	non-linear tangent stiffness parameter
κ	gradient of the unload-reload line (URL)
λ	gradient of the normal compression line (NCL)
μ	strain influence distribution function
σ'_v	vertical effective stress
σ'_{v0}	initial geostatic vertical effective stress
$\sigma'_{v,eqm}$	equilibrium vertical effective stress
$\sigma'_{v,NCL}$	vertical effective stress on the NCL
$\sigma'_{v,RSL}$	vertical effective stress on the remoulded state line (RSL)
Φ	lumped strength parameter

REFERENCES

- Andersen, K. H. (2015). Cyclic soil parameters for offshore foundation design. In *Frontiers in offshore geotechnics III* (ed. V. Meyer), pp. 3–82. London, UK: Taylor & Francis Group.
- Andersen, K. H., Kleven, A. & Heien, D. (1988). Cyclic soil data for design of gravity structures. *J. Geotech. Engng* **114**, No. 5, 517–539.
- Aubeny, C. (2018). *Geomechanics of marine anchors*. Boca Raton, FL, USA: CRC Press.
- Blake, A. & O'Loughlin, C. D. (2015). Installation of dynamically embedded plate anchors as assessed through field tests. *Can. Geotech. J.* **52**, No. 9, 1270–1282.
- Blake, A. P., O'Loughlin, C. D. & Gaudin, C. (2010). Setup following keying of plate anchors assessed through centrifuge tests in kaolin clay. In *Frontiers in offshore geotechnics II* (eds S. Gourvenec and D. J. White), pp. 705–710. Boca Raton, FL, USA: CRC Press/Balkema.
- Boussinesq, J. (1885). *Application des potentiels à l'étude de l'équilibre et du mouvement des solides élastiques: mémoire suivi de notes étendues sur divers points de physique mathématique et d'analyse*. Paris, France: Gauthier-Villars (in French).
- Brown, R. P., Wong, P. C. & Audibert, J. M. (2010). SEPLA keying prediction method based on full-scale offshore tests. In *Frontiers in offshore geotechnics II* (eds S. Gourvenec and D. J. White), pp. 717–722. Boca Raton, FL, USA: CRC Press/Balkema.
- Cassidy, M. J., Gaudin, C., Randolph, M. F., Wong, P. C., Wang, D. & Tian, Y. (2012). A plasticity model to assess the keying of plate anchors. *Géotechnique* **62**, No. 9, 825–836, <https://doi.org/10.1680/geot.12.OG.009>.
- Chang, K., Hossain, M. S., Kim, Y. H. & Wang, D. (2019). Cyclic capacity and diving potential of novel fish anchor in calcareous silt. *ASCE J. Geotech. Geoenviron. Engng* **145**, No. 9, [https://doi.org/10.1061/\(ASCE\)GT.1943-5606.0002095](https://doi.org/10.1061/(ASCE)GT.1943-5606.0002095).
- Chatterjee, S., White, D. J. & Randolph, M. F. (2013). Coupled consolidation analysis of pipe–soil interactions. *Can. Geotech. J.* **50**, No. 6, 609–619.
- Chow, S. H., O'Loughlin, C. D., Zhou, Z., White, D. J. & Randolph, M. F. (2019). Penetrometer testing in a calcareous silt to explore changes in soil strength. *Géotechnique*, <https://doi.org/10.1680/jgeot.19.P069>.
- Chung, S. F. & Randolph, M. (2004). Penetration resistance in soft clay for different shaped penetrometers. In *Geotechnical and geophysical site characterization* (eds A. V. da Fonseca and P. W. Mayne), pp. 671–677. Amsterdam, the Netherlands: IOS Press.
- Cocjin, M. L., Gourvenec, S. M., White, D. J. & Randolph, M. F. (2014). Tolerably mobile subsea foundations—observations of performance. *Géotechnique* **64**, No. 11, 895–909, <https://doi.org/10.1680/geot.14.P098>.
- Colreavy, C., O'Loughlin, C. D. & Randolph, M. F. (2016). Experience with a dual pore pressure element piezoball. *Int. J. Phys. Modelling Geotech.* **16**, No. 3, 101–118.
- Dahlberg, R. & Strøm, P. J. (1999). Unique onshore tests of deepwater drag-in plate anchors. *Proceedings of the offshore technology conference*, Houston, TX, USA, paper OTC 10989.
- Einav, I. & Randolph, M. F. (2005). Combining upper bound and strain path methods for evaluating penetration resistance. *Int. J. Numer. Methods Engng* **63**, No. 14, 1991–2016.
- Gaudin, C., O'Loughlin, C. D., Randolph, M. & Lowmass, A. C. (2006). Influence of the installation process on the performance of suction embedded plate anchors. *Géotechnique* **56**, No. 6, 381–391, <https://doi.org/10.1680/geot.2006.56.6.381>.
- Gourvenec, S. & Randolph, M. F. (2010). Consolidation beneath circular skirted foundations. *Int. J. Geomech.* **10**, No. 1, 22–29.
- Grieves, M. & Vickers, J. (2017). Digital twin: mitigating unpredictable, undesirable emergent behavior in complex systems. In *Transdisciplinary perspectives on complex systems* (eds F. J. Kahlen, S. Flumerfelt and A. Alves), pp. 85–113. Cham, Switzerland: Springer.
- Han, C. (2016). *Performance of plate anchors under sustained loading*. PhD thesis, The University of Western Australia, Perth, Australia.
- Heyerdahl, H. & Eklund, T. (2001). Testing of plate anchors. *Proceedings of the offshore technology conference*, Houston, TX, USA, paper OTC 13273.
- Hodder, M., White, D. J. & Cassidy, M. J. (2009). Effect of remolding and reconsolidation on the touchdown stiffness of a steel catenary riser: observations from centrifuge modelling. *Proceedings of the offshore technology conference*, Houston, TX, USA, paper no. OTC 19871.
- House, A., Olivera, J. R. M. S. & Randolph, M. F. (2001). Evaluating the coefficient of consolidation using penetration tests. *Int. J. Phys. Modelling Geotech.* **1**, No. 3, 17–25.
- Liu, J., Tan, M. & Hu, Y. (2018). New analytical formulas to estimate the pullout capacity factor for rectangular plate anchors in NC clay. *Appl. Ocean Res.* **75**, 234–247.
- Mahmoodzadeh, H., Wang, D. & Randolph, M. F. (2015). Interpretation of piezoball dissipation testing in clay. *Géotechnique* **65**, No. 10, 831–842, <https://doi.org/10.1680/jgeot.14.P213>.
- Martin, C. M. & Randolph, M. F. (2001). Application of the lower bound and the upper bound theorems of plasticity to collapse of circular foundations. In *Computer methods and advances in geomechanics* (eds C. Desai, T. Kundu, S. Harpalani, D. Contractor and J. Kemeny), vol. 2, pp. 1417–1428. Boca Raton, FL, USA: CRC Press/Balkema.
- Martin, C. M. & Randolph, M. (2006). Upper-bound analysis of lateral pile capacity in cohesive soil. *Géotechnique* **56**, No. 2, 141–145, <https://doi.org/10.1680/geot.2006.56.2.141>.
- O'Loughlin, C. D., Blake, A., Richardson, M. D., Randolph, M. & Gaudin, C. (2014). Installation and capacity of dynamically

- embedded plate anchors as assessed through centrifuge tests. *Ocean Engng* **88**, 204–213.
- O'Loughlin, C. D., White, D. J. & Stanier, S. A. (2015). Novel anchoring solutions for FLNG – opportunities driven by scale. *Proceedings of the offshore technology conference*, Houston, TX, USA, paper OTC 26032.
- O'Loughlin, C. D., Blake, A. P. & Gaudin, C. (2016). Towards a simple design procedure for dynamically embedded plate anchors. *Géotechnique* **66**, No. 9, 741–753, <https://doi.org/10.1680/jgeot.15.P209>.
- O'Loughlin, C. D., White, D. J. & Stanier, S. A. (2017). Plate anchors for mooring floating facilities – a view towards unlocking cost and risk benefits. In *Offshore site investigation and geotechnics 2017 conference proceedings*, vol. 2, pp. 978–986. London, UK: Society for Underwater Technology.
- O'Loughlin, C. D., Neubecker, S. & Gaudin, C. (2018). Anchoring systems: anchor types, installation, and design. In *Encyclopedia of maritime and offshore engineering* (eds J. Carlton, P. Jukes and Y. S. Choo). Hoboken, NJ, USA: John Wiley & Sons, <https://doi.org/10.1002/9781118476406.emoe534>.
- Poulos, H. G. & Davis, E. H. (1974). *Elastic solution for soil and rock mechanics*. Hoboken, NJ, USA: John Wiley & Sons.
- Randolph, M. F. & Hope, S. N. (2004). Effect of cone velocity on cone resistance and excess pore pressure. In *Proceedings of conference on engineering practice and performance of soft deposits* (eds T. Matsui, Y. Tanaka and M. Mimura), pp. 147–152. Osaka, Japan: Yodogawa Kogisha Co. Ltd.
- Randolph, M. F., Jewell, R. J., Stone, K. J. & Brown, T. A. (1991). Establishing a new centrifuge facility. In *Centrifuge '91: proceedings of the international conference on centrifuge modelling* (eds H. Y. Ko and F. G. McLean), pp. 3–9. Rotterdam, the Netherlands: Balkema.
- Renzi, D., Maniar, D., McNeill, S. & Del Vecchio, C. (2017). Developing a digital twin for floating production systems integrity management. *Proceedings of the offshore technology conference (OTC Brasil)*, Rio de Janeiro, Brazil, paper OTC-28012-MS.
- Sharma, P., Hamedifar, H., Brown, A. & Green, R. (2017). The Dawn of the new age of the industrial internet and how it can radically transform the offshore oil and gas industry. *Proceedings of the offshore technology conference*, Houston, TX, USA, paper no. OTC-27638-MS.
- Stanier, S. A. & White, D. J. (2019). Enhancement of bearing capacity from consolidation: due to changing strength or failure mechanism? *Géotechnique* **69**, No. 2, 166–173, <https://doi.org/10.1680/jgeot.17.T030>.
- Stewart, D. P. & Randolph, M. F. (1991). A new site investigation tool for the centrifuge. In *Centrifuge '91: proceedings of the international conference on centrifuge modelling* (eds H. Y. Ko and F. G. McLean), pp. 531–538. Rotterdam, the Netherlands: Balkema.
- Teh, C. I. & Houlsby, G. T. (1991). An analytical study of the cone penetration test in clay. *Géotechnique* **41**, No. 1, 17–34, <https://doi.org/10.1680/geot.1991.41.1.17>.
- Vryhof (Vryhof Anchors) (2006). *Vryhof anchor manual 2006*. Schiedam, the Netherlands: Vryhof Anchors BV.
- Wang, D. & O'Loughlin, C. D. (2014). Numerical study of pull-out capacities of dynamically embedded plate anchors. *Can. Geotech. J.* **51**, No. 11, 1263–1272.
- Wang, D., Hu, Y. & Randolph, M. (2010). Three-dimensional large deformation finite-element analysis of plate anchors in uniform clay. *J. Geotech. Geoenviron. Engng* **136**, No. 2, 355–365.
- Wang, D., Gaudin, C. & Randolph, M. (2013). Large deformation finite element analysis investigating the performance of anchor keying flap. *Ocean Engng* **59**, 107–116.
- Wilde, B., Treu, H. & Fulton, T. (2001). Field testing of suction embedded plate anchors. In *Proceedings of the 11th ISOPE conference*, Stavanger, Norway, vol. 2, pp. 544–551. Mountain View, CA, USA: International Society of Polar and Offshore Engineers.
- Wong, P., Gaudin, C., Randolph, M., Cassidy, M. & Tian, Y. (2012). Performance of suction embedded plate anchors in permanent mooring applications. In *Proceedings of the 22nd international offshore and polar engineering conference*, Rhodes, Greece, pp. 640–645. Mountain View, CA, USA: International Society of Polar and Offshore Engineers.
- Yu, L., Liu, J., Kong, X. J. & Hu, Y. (2011). Numerical study on plate anchor stability in clay. *Géotechnique* **61**, No. 3, 235–246, <https://doi.org/10.1680/geot.8.P071>.
- Yu, S. B., Hambleton, J. P. & Sloan, S. W. (2015). Undrained uplift capacity of deeply embedded strip anchors in non-uniform soil. *Comput. Geotech.* **70**, 41–49.
- Zhou, Z., White, D. J. & O'Loughlin, C. D. (2019a). An effective stress framework for estimating penetration resistance accounting for changes in soil strength from maintained load, remoulding and reconsolidation. *Géotechnique* **69**, No. 1, 57–71, <https://doi.org/10.1680/jgeot.17.P217>.
- Zhou, Z., White, D. J. & O'Loughlin, C. D. (2019b). The changing strength of soft soils: parallel penetrometer and foundation tests with cyclic loading and reconsolidation periods. *Can. Geotech. J.* (in press).